Acta Materialia 258 (2023) 119229

Contents lists available at ScienceDirect

Acta Materialia

journal homepage: www.elsevier.com/locate/actamat

High-temperature active oxidation of nanocrystalline silicon-carbide: A reactive force-field molecular dynamics study

Luc Capaldi [a], Frederic Sansoz [a,b,*]

[a] Department of Mechanical Engineering, The University of Vermont, 33 Colchester Avenue, Burlington, VT 05405, USA
[b] Materials Science Program, The University of Vermont, Burlington, VT, USA

ARTICLE INFO

Keywords:
Nanocrystalline
Silicon-carbide ceramic
Oxidation kinetics
Passive-to-active oxidation mechanisms

ABSTRACT

Flexible woven SiC ceramics are prone to accelerated fiber embrittlement under high temperature oxidation in dynamic oxygen environments. The nanocrystalline structure of the constituent fibers impacts the reaction kinetics and phase transformations during active oxidation. However, fundamental understanding and quantification of grain boundary effects on oxidation behavior in nanocrystalline SiC remain elusive when temperatures exceed 1500 K. This study deploys large-scale molecular dynamics simulations with a reactive force-field to elucidate the complex roles of atomic oxygen reservoir conditions and grain size on oxidation kinetics and the nature of oxides produced in both monocrystalline and nanocrystalline 3C-SiC between 1100 K and 2000 K. The simulations with dynamically replenished oxygen provide good agreement with oxidation kinetics and activation energies for the monocrystalline Si(100) and C(100) orientations published in the available literature. This study reveals that, by contrast, nanocrystalline SiC samples exhibit two distinct oxidation kinetics with a transition point at 1500 K due to surface melting, which is supported by experimental evidence. The introduction of a grain-boundary network produces a two-fold decrease in oxidation activation energies compared to monocrystalline SiC below 1500 K. Above 1500 K, however, the activation energies rise substantially due to the formation of a liquid Si phase at the SiC/Si oxide interface. It is shown that the stability of the interfacial liquid phase is promoted by incoherent grain boundaries in the crystalline SiC. These findings are important for the deployment of nanocrystalline SiC fibers in advanced thermal protection systems for high-temperature applications.

1. Introduction

Due to its wide band gap and favorable neutronics, SiC offers a well-documented and versatile set of physical and mechanical properties that are relevant to the nuclear [1] and semiconductor manufacturing [2] sectors. In addition, its high thermal stability, strength, and fracture toughness [3] at elevated temperature generate equal interest for thermal protection systems (TPS) shielding spacecrafts from a variety of high-enthalpy, chemically reactive, disassociated hypersonic flows during atmospheric entry [4,5]. Notably, SiC woven fibers have emerged as primary materials for the shell of modern flexible TPS [6], because recent TPS developments for planetary missions by NASA have shifted towards lightweight deployable structures composed of multiple flexible insulators sheathed by a thermally resistant woven ceramic fabric [7]. Interestingly, a similar technology is deployed in emergency wildfire shelters for first responders, serving as the final defense against flame entrapment [8,9]. These flexible TPS must withstand immense thermal loads, with wildfire temperatures typically ranging in excess of 1070 K to 1470 K [10], while TPS for the Space Shuttle Orbiter reportedly reached up to 1921 K during re-entry in the Earth atmosphere [11].

To provide motivation for the current work, Fig. 1 presents high-resolution scanning electron microscopy images of representative Hi-Nicalon SiC woven fibers used for flexible TPS in hypersonic inflatable aerodynamic heat shields [6,12]. Nominally, Hi-Nicalon fibers contain oxygen concentrations less than 1.2 wt.%, because their microstructure is comprised of 3C-SiC nanocrystals that are separated by intergranular free carbon and a silicon oxycarbide phase [13]. In this instance, the fibers have been exposed to a high-enthalpy oxygen plasma at a temperature of 1573 K using an inductively coupled plasma torch that simulates hypersonic atmospheric entry environments [14]. Chemical analysis of fibers in Fig. 1 indicates an oxygen content of 32 wt.%, which corresponds to a 30-fold increase from its nominal value due to

* Corresponding author at: Department of Mechanical Engineering, The University of Vermont, 33 Colchester Avenue, Burlington, VT 05405, USA.
E-mail address: frederic.sansoz@uvm.edu (F. Sansoz).

https://doi.org/10.1016/j.actamat.2023.119229
Received 2 May 2023; Received in revised form 1 August 2023; Accepted 6 August 2023
Available online 7 August 2023

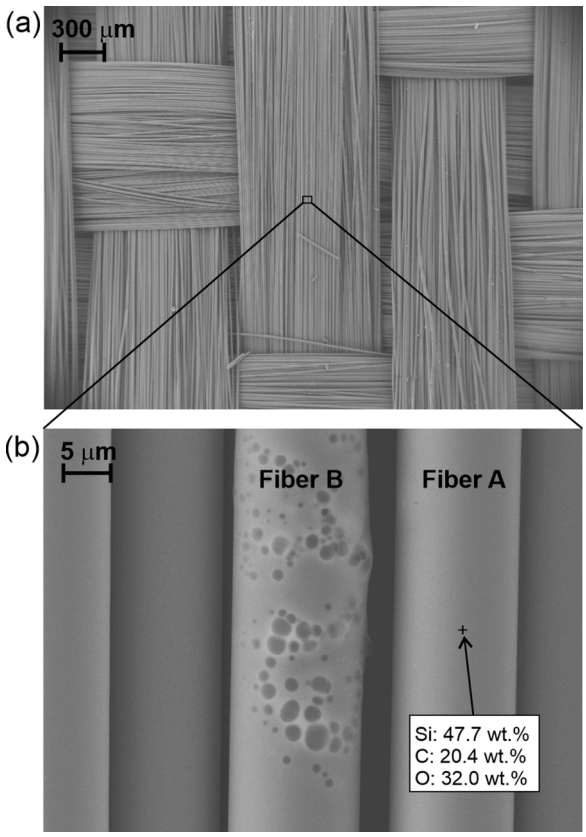

Fig. 1. Field-emission scanning electron microscopy images of woven nanocrystalline Hi-Nicalon SiC fibers after thermal exposure to a high-enthalpy oxygen plasma at 1573 K tested in a previous study by Owens et al. [14]. The inset indicates the chemical composition of Fiber A obtained from electron dispersive x-ray spectroscopy. It should be noted that Fiber B has formed surface gas bubbles suggesting the occurrence of local surface melting under such extreme high-temperature environments.

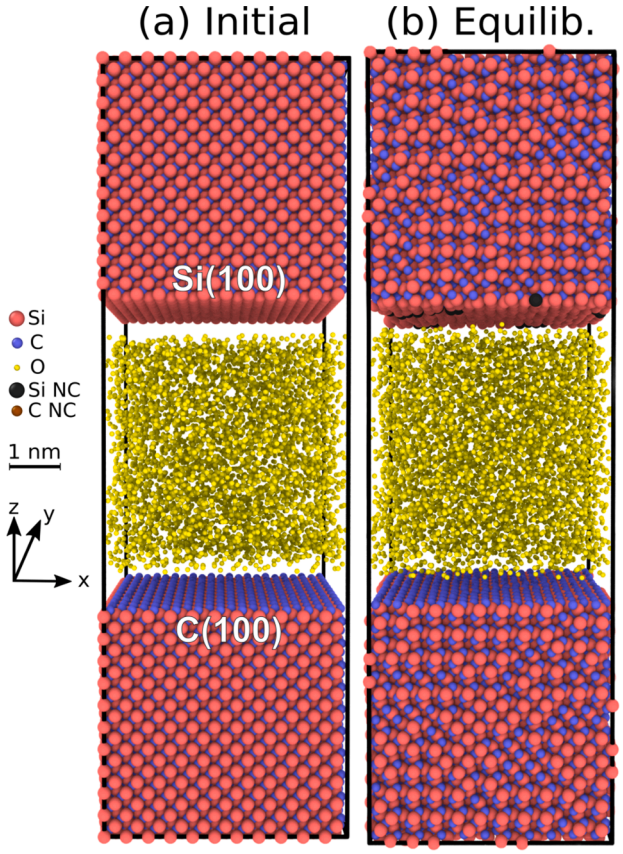

Fig. 2. Atomistic models of 3C-SiC monocrystals with free surfaces parallel to either the Si(100) or C(100) planes in their (a) initial and (b) equilibrated configurations. Different colors are used to differentiate perfectly crystalline and non-crystalline (NC) atoms, respectively.

oxidation. Furthermore, the occurrence of gas bubbles formed on the surface of some fibers suggests that combined high heat flux and oxygen content led to local surface melting at temperatures well below the SiC melting point (3100 K). Here, we use this experimental evidence to underscore the importance of understanding the fundamental mechanisms of active oxidation in nanocrystalline SiC fibers under such extreme thermal environments. Several experimental and computational studies [15,16] have emphasized a pronounced dependence of the underlying chemical reactions and passive-to-active oxidation transitions on temperature and oxygen pressure in SiC monocrystals. However, current oxidation models have so far little predictive power for determining how grain boundaries influence the complex surface oxidation kinetics and phase transformations in nanocrystalline SiC fibers at high temperature.

Herein, this study uses large-scale molecular dynamics (MD) simulations with a reactive force field (ReaxFF) to quantify chemical reactions and oxidation kinetics in both monocrystalline and nanocrystalline 3C-SiC exposed to atomic oxygen in the 1100 K – 2000 K range. An improved MD simulation technique, integrating different oxygen reservoir conditions and a self-consistent analysis of oxide growth, is developed, and validated against available literature data on monocrystalline SiC oxidation. This methodology is subsequently extended to two nanocrystalline SiC samples of 5 nm and 10 nm in average grain size, respectively, to examine the effects of a grain-boundary network on temperature-dependent oxidation kinetics and associated surface oxidation mechanisms at the atomic scale. Furthermore, we discuss the experimental observations made in Fig. 1 from the perspective of temperature-dependent chemical reactions predicted in our simulations. The present study is the first to systematically examine the effects of a grain-boundary network on active oxidation kinetics in SiC with grains on the order of 5–10 nm [17].

2. Methods

2.1. MD simulations

MD simulations of 3C-SiC oxidation were performed using the Large-scale Atomic/Molecular Massively Parallelized Simulator (LAMMPS) [18] with the ReaxFF potential for the Si/O/C/H/N system developed by Vashisth et al. [19] via optimization of the CHON-2017_weak force field [20] with datasets from Pitman et al. [21] for Si/O/H interactions and Newsome et al. [6] for C/O/Si interactions. Although recently introduced, this potential has been shown to accurately reproduce chemical interactions in the SiC/O system [22,23,19]. We also note that the description of Si-C interactions (which in turn defines the melting temperature and other material properties) follows directly from the work of Newsome et al. [16], which has been applied extensively in prior reactive SiC studies. Two monocrystalline materials with free surfaces parallel to the Si(100) and C(100) planes, respectively, were simulated as a pair for computing efficiency. A spatially continuous oxygen reservoir was used to oxidize both surfaces simultaneously, as shown in Fig. 2. The model was created using the software Atomsk [24] with an initial size of 15 nm with shrink-wrapped boundaries in the z-direction, a cross-sectional area of 4.8 nm $\times$ 4.8 nm and periodic boundaries in the x- and y-directions. The specified cross-sectional area was found to adequately minimize atomic fluctuations. The oxygen

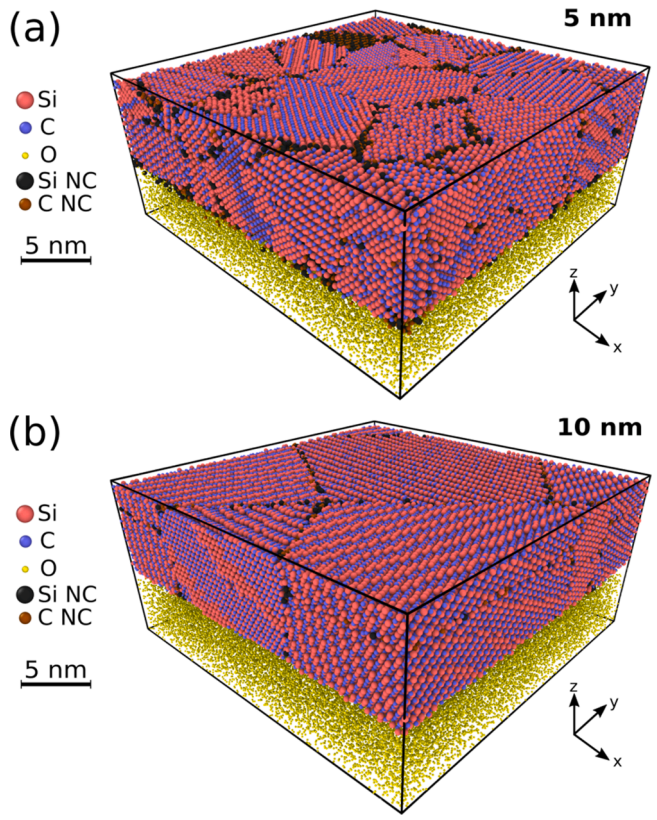

Fig. 3. Atomistic models of 3C-SiC nanocrystalline samples with an average grain diameter of (a) 5 nm and (b) 10 nm. Non-crystalline (NC) Si and C atoms are highlighted to reveal the grain-boundary microstructure [29].

region had a length of 4.7 nm in the z-direction, uniformly filled with randomly oriented atomic oxygen with a number density of 40 atoms/nm^3, corresponding to an oxygen partial pressure of 168.05 MPa at 300 K and 1120.34 MPa at 2000 K. Atomic oxygen was specifically selected to replicate the dissociated oxygen encountered in atmospheric re-entry environments. A high gas pressure was used to enable adequate chemical reactions to occur during the short MD timescale, in line with previous MD simulation studies using reactive force fields [16,25–28].

Furthermore, Atomsk [24] was used to construct nanocrystalline 3C-SiC films with dimensions of 20 nm × 20 nm × 5 nm in the x, y, z directions, as shown in Fig. 3. Relevant heat-resistant SiC fibers employed in TPS, such as Hi-Nicalon fibers, are characterized by a nanocrystalline structure with average grain diameters ranging from 5 to 50 nm [14,13,17]. Here, the simulated SiC nanocrystals had average grain diameters of 5 nm and 10 nm. An oxygen region with the same dimensions was introduced to the bottom face of each nanocrystalline sample, populated with atomic oxygen, and contained with a reflective barrier. The diamond structure identification in the Open Visualization Tool (OVITO) [30] was used to differentiate atoms from crystalline and non-crystalline (NC) phases.

All models, including both atomic oxygen and SiC atoms, were prepared using the same methodology reported by Liu et al. [25] to produce relaxed GB structures. First, the energy and force were minimized by conjugate-gradient method to a threshold of 1×10^{-6}, respectively. Reflective walls were used to prevent Si or C atoms from entering the oxygen region prematurely. The models were equilibrated at 300 K for 2.5 ps in the canonical ensemble (NVT) with a Nose-Hoover thermostat using a temperature damping coefficient of 25 fs and a timestep of 0.25 fs. To improve stability, 0.5 nm-thick layers of SiC atoms at the top and bottom of the simulation box had their atomic velocity changed to freeze the boundaries to a constant temperature of 0.01 K after the initial energy minimization [25]. We note, however, that these frozen boundaries were free to move to account for thermal expansion in the z-direction. Atoms outside the frozen boundaries were equilibrated at 300 K in NVT for 2.5 ps, heated to 500 K at a rate of 120 K/ps, relaxed for 2.5 ps, cooled to 300 K at the same rate, and quenched in the isobaric-isothermal ensemble (NPT) at 300 K and 0 Pa for 2.5 ps. Finally, the system was equilibrated in NVT at 300 K for 2.5 ps, heated to the target temperature at a rate of 120 K/ps, and annealed at this temperature for 200 ps.

2.2. Oxide growth analysis

Previous MD simulation studies have either allowed the available oxygen to deplete over the simulation [16,25,26,31], or included a very large reservoir to maintain constant gas flow [28]. Alternatively, in the present study, atomic oxygen atoms were introduced to the system dynamically in response to the depletion rate. This was achieved by defining an oxygen source region that occupies the oxygen reservoir up to 1.5 nm from the SiC surface to ensure that atoms are never added directly to the oxide film. The number of depleted atomic oxygen atoms were introduced at random positions within the oxygen source region every 0.1 ps and their velocities are scaled to maintain constant reservoir temperature and pressure. Once again, atomic oxygen was selected to better replicate the atmospheric re-entry environment. The ReaxFF potential was used to monitor the bond formation and break up. A maximum of eight bonds per atom were allowed, with a coarse bond order cutoff of 0.300. The bond count over time was linearly converted to the corresponding oxide thickness using Eq. (1) [32].

$$X = \frac{\Delta m (M_{SiO2}/\dot{M}_{SiO2})}{\rho_{SiO2}\, A} \tag{1}$$

where X is the oxide thickness, Δm is the mass change measured from the number of oxygen atoms within the SiO_2 phase, M_{SiO2} is the molecular weight of SiO_2, $\dot{M}_{SiO2}$ is the molecular weight gain per mole of SiO_2 formed, ρ_{SiO2} is the density of SiO_2 and A is the surface area. The oxide growth rate was quantified using the Massoud model of oxidation given by Eq. (2) [33].

$$\frac{dX}{dt} = \frac{B}{A + 2X} + C\ exp\left(-\frac{X}{L}\right) \tag{2}$$

where B/A is the linear rate constant, B is the parabolic rate constant, C is the pre-exponential constant and L is the characteristic length. This empirical model improves on the classical linear-parabolic Deal-Grove model of oxidation to properly describe oxide films smaller than ~ 30 nm. However, simulations of SiC have revealed very early-stage oxide growth (< 1 nm) with logarithmic-linear time dependence [25], which is not efficiently captured by this model. Therefore, it serves as a convenient method for empirically quantifying the oxide growth rate, but the fitting parameters cannot be reliably compared to prior studies. All fitting parameters are provided as Supplementary Tables S1–S4. Since an analytical solution is not available, the Optimization Toolkit in the software Matlab R2021a (MathWorks Inc., Natick, MA) was used to numerically approximate solutions using the 4th Order Runge-Kutta method. The result was subsequently treated as a nonlinear minimization problem and positive model coefficients were iteratively fitted to the data using the Trust Region Reflective Algorithm until a constraint tolerance of 1×10^{-6} was achieved [34]. Arrhenius parameters were calculated for each exposed face by fitting the computed growth rates at a constant oxide thickness and minimizing the fit error.

2.3. Experimental characterization

Nanocrystalline Hi-Nicalon woven SiC fibers (COI Ceramics, Inc, USA) were examined experimentally in this study. The fibers were distributed in the form of tows, which were untwisted bundles of

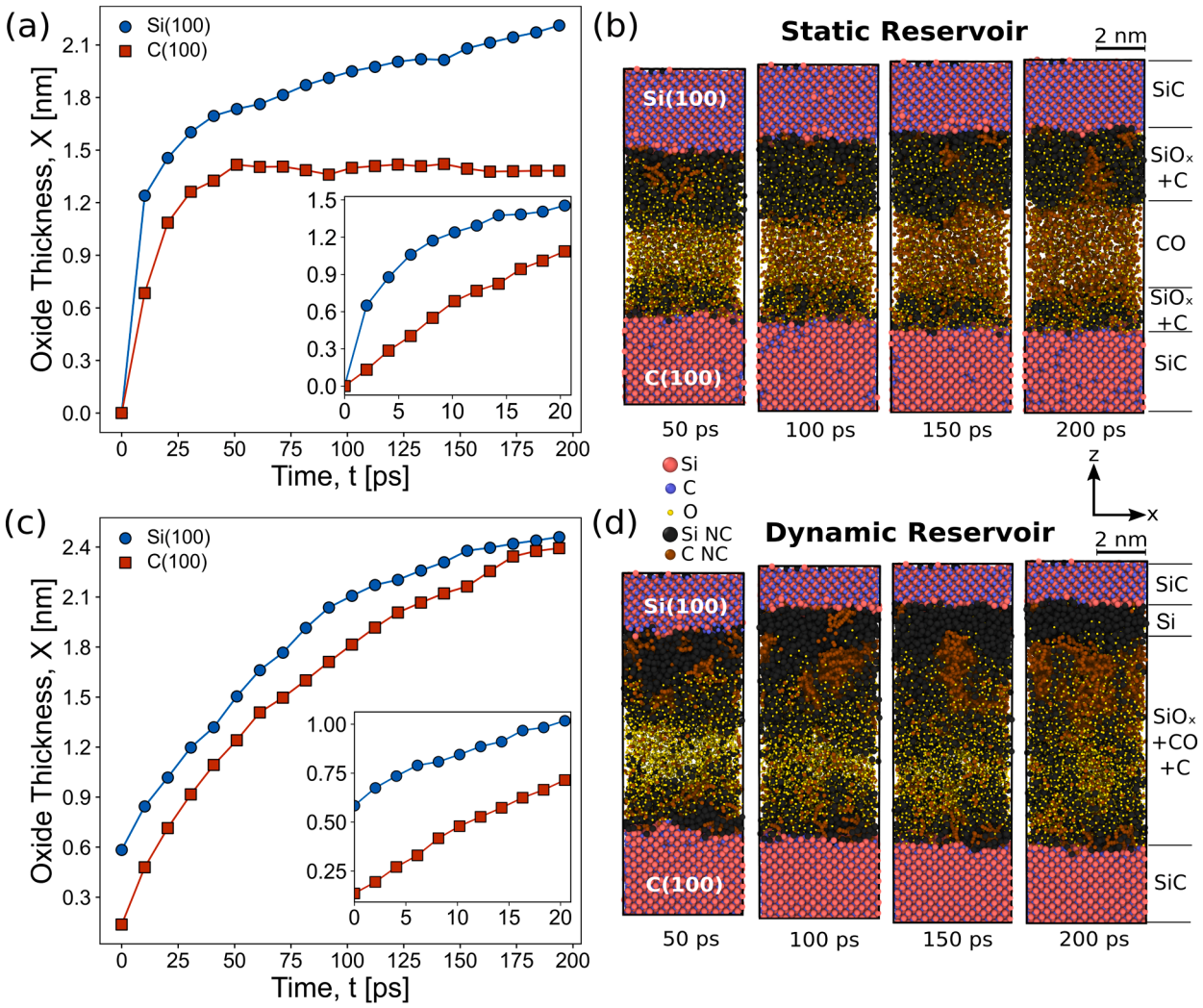

Fig. 4. Simulations of 3C-SiC monocrystals at 2000 K with differing oxygen reservoir conditions. Time-dependent oxide thickness and periodic simulation snapshots are presented for the cases of (a,b) static reservoir and (c,d) dynamic reservoir with oxygen addition. Insets in (a,c) show the trajectories during the first 20 ps of simulation.

parallel, continuous filaments of 14 μm in diameter [35]. The SiC tows formed a cloth with a 5-harness satin weave having 26 fibers per inch in both the warp and weft directions, with each fiber overlapping 4 cross fibers before being woven under 1 cross fiber. The woven cloth was exposed to a pure oxygen plasma at a heat flux of 79 W/cm^2 for 240 s by Owens et al. [14]. Surface temperatures were recorded *in situ* using a Marathon Series MR1SACF and MR1SCCF infrared pyrometer (600 °C–3000 °C range) operating with a 0.75–1.1 μm wavelength range. Surface temperatures in pure oxygen plasma remained constant at 1573 ± 50 K. Microstructure and chemical characterizations were carried out after plasma exposure by field-emission scanning electron microscopy (Sigma 300 VP, Zeiss, Germany) and electron dispersive x-ray spectroscopy (Oxford Instruments, United Kingdom), respectively.

3. Results

3.1. Monocrystalline oxide growth

Our simulations reveal that the time evolution of oxide thickness is highly dependent upon the conditions within the oxygen reservoir. Fig. 4(a,b) shows the results of a 2000 K static reservoir, which is the same as that employed in previous MD simulation studies [25]. Under this reservoir condition, the oxide thickness grows rapidly during the initial stage of oxidation as shown in the inset of Fig. 4a. Si-C bonds break to form new Si-O and C-O bonds, but also non-crystalline C-C ones. After the initial uptake, the chemistry of the final configuration at 200 ps in Fig. 4b reveals that a gas of CO molecules separates distinctively from the SiOx + C phase. This result suggests that the transport of O atoms through this oxide phase limits the oxidation reaction at the SiC interface. This hypothesis is supported by the more moderate trajectories shown in the latter portion of the curves in Fig. 4a, which are the same as logarithmic-linear trajectories found in prior computational work [16, 25]. Furthermore, Fig. 4b shows that the oxidation rate on the C(100) face is partially suppressed, compared to the Si(100) one. This observation reveals that a static oxygen reservoir condition is not viable for multi-grain simulations, because the surface characteristics of certain orientations artificially dominate the reaction with the available reactants.

A more realistic reservoir is instead shown in Fig. 4(c,d) and Supplementary Movie S1, wherein the oxygen is replenished dynamically at a time-varying rate that preserves the concentration of O atoms in the gas reservoir. During the first 20 ps of the simulation, this change reduces the initial uptake of O because the reaction products are less readily transported away from the crystal surface. Over the entire simulation, however, the dynamic oxygen reservoir enabled us to reach maximum oxide thicknesses that are 9.3% and 77.7% larger than the

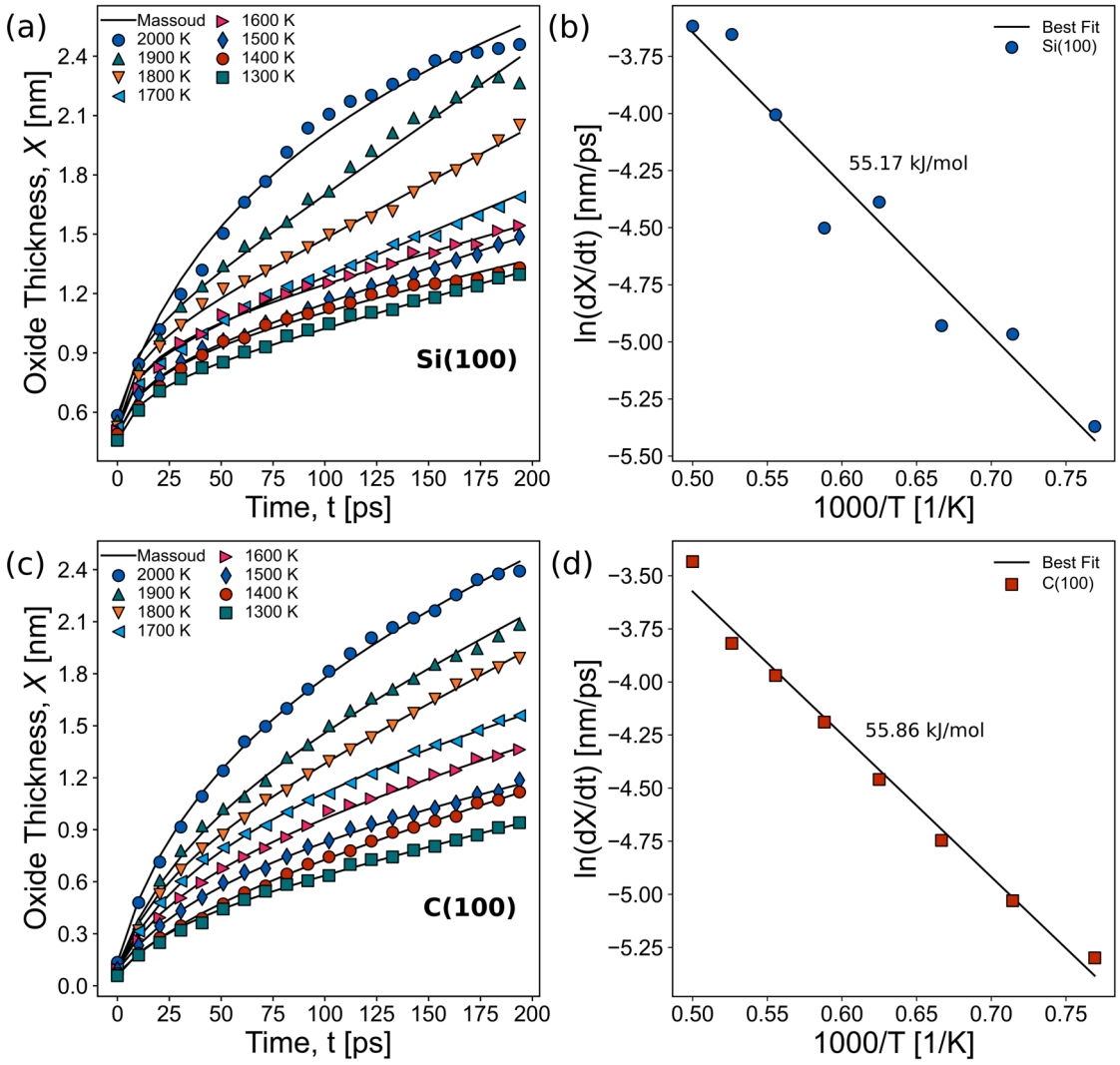

Fig. 5. Temperature-dependent oxidation results and Arrhenius analysis for the Si(100) and C(100) monocrystals.

static reservoir for the Si(100) and C(100) faces, respectively. The large relative increase in oxide thickness for the C(100) face confirms a pronounced influence of the gas reservoir conditions in these simulations. The chemistry of the final configuration at 200 ps in Fig. 4d shows that the central region is quickly occupied by a mix of SiOx, CO, O, and clumped C chains. More importantly, a salient feature found in Fig. 4d is that a non-crystalline melted region of pure Si has formed at the interface between crystalline SiC and SiOx oxides at 2000 K, which is absent in the case of the static reservoir. This prediction suggests that the dynamic gas reservoir initiates a phase transformation that was not directly observed with the static reservoir but is physically meaningful, considering our experimental observation of surface melting in nanocrystalline Hi-Nicalon fibers in Fig. 1.

The temperature dependence of oxide thickness and oxidation rates in the monocrystalline SiC model with dynamically replenished oxygen is studied in Fig. 5 for different temperatures ranging from 1300 K to 2000 K. The trajectories and Massoud model fits are shown in Fig. 5(a,c) for the Si(100) and C(100) monocrystals, respectively. The corresponding Arrhenius analysis is shown in Fig. 5(b,d), with $R^2 > 95\%$ in both cases; activation energies of 55.17 kJ/mol and 55.86 kJ/mol are obtained for the Si(100) and C(100) monocrystals, respectively. Arrhenius analyses in prior computational studies of 3C-SiC oxidation (in dry O_2) have provided parameters that varied significantly within the literature. For example, for the Si(100) orientation, activation energies measured computationally spanned from 35.6 to 86.4 kJ/mol [26,27,36]. The values reported herein conform to the computational literature but also are generally smaller than the experimental ones. For example, Wilson and Opila [32] have comprehensively reviewed experimental data on SiC fiber oxidation in differing environments and reported activation energies ranging from 69 to 249 kJ/mol for parabolic oxidation and from 72 to 192 kJ/mol for linear oxidation [32], which agrees with the most recent experiments [37]. In the present study, two effects may contribute to this outcome: (i) the inclusion of atomic rather than molecular oxygen, (ii) the reaction kinetics themselves. A lower activation energy is expected for reaction-limited oxidation, suggesting that our simulations are physically accurate.

3.2. *Nanocrystalline oxide growth*

The simulation trajectories and Arrhenius analysis for 5-nm and 10-nm nanocrystalline SiC models are presented in Fig. 6(a,b) and 6(c,d), respectively. Contrary to the single regime predicted in monocrystal simulations, two distinct oxidation regimes are observed in nanocrystalline SiC, with a temperature transition estimated at $T \sim 1500$ K or $1000/T \sim 0.66$. Although the melting temperature was not explicitly characterized in this work, the transition temperature is consistent with our experimental observations of local fiber surface melting that occurs prior to 1573 K. Furthermore, classical potentials (e.g., Vashishta,

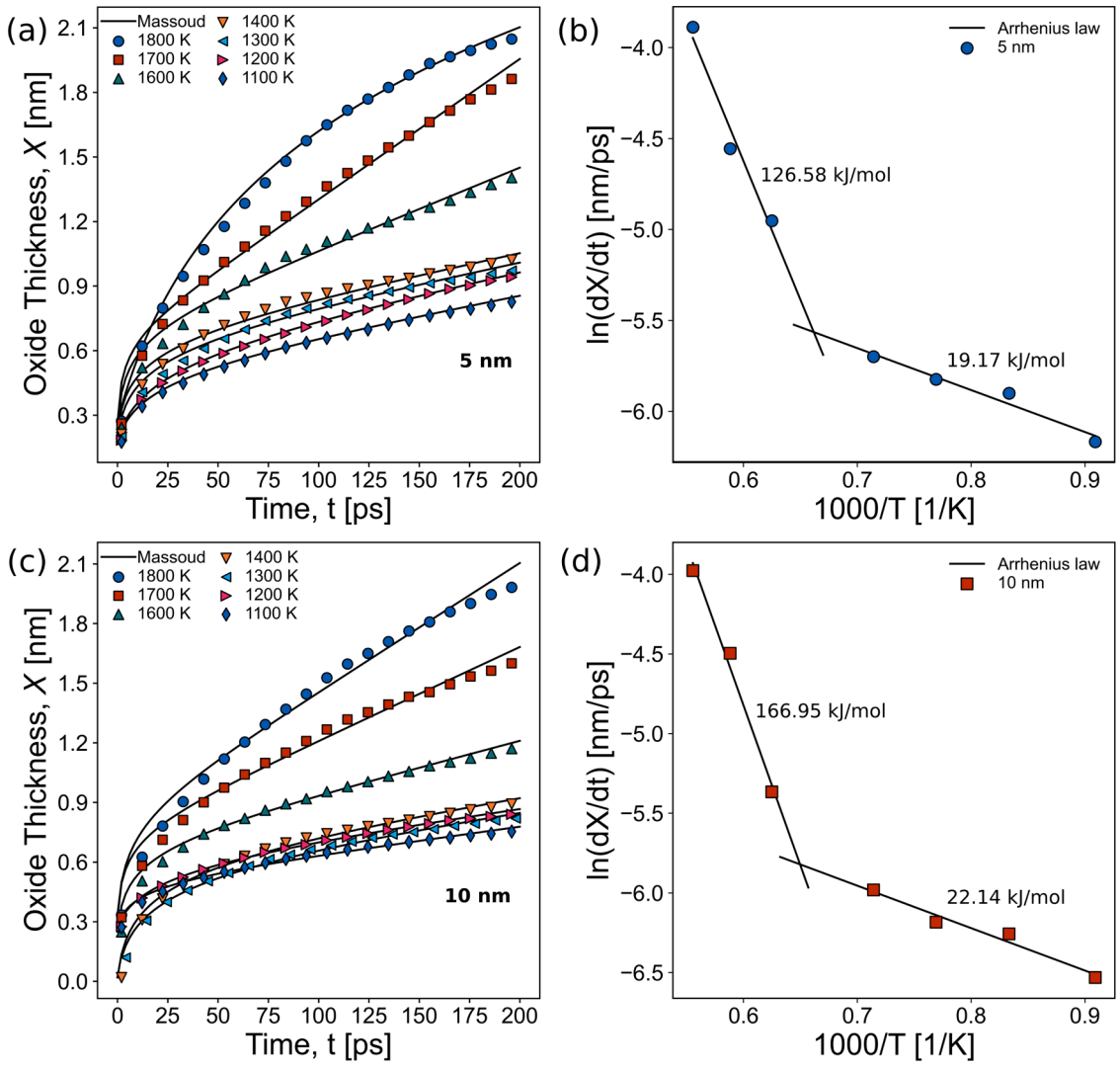

Fig. 6. Temperature-dependent oxidation results and Arrhenius analysis for nanocrystalline SiC films with grain diameters of 5 nm and 10 nm, respectively.

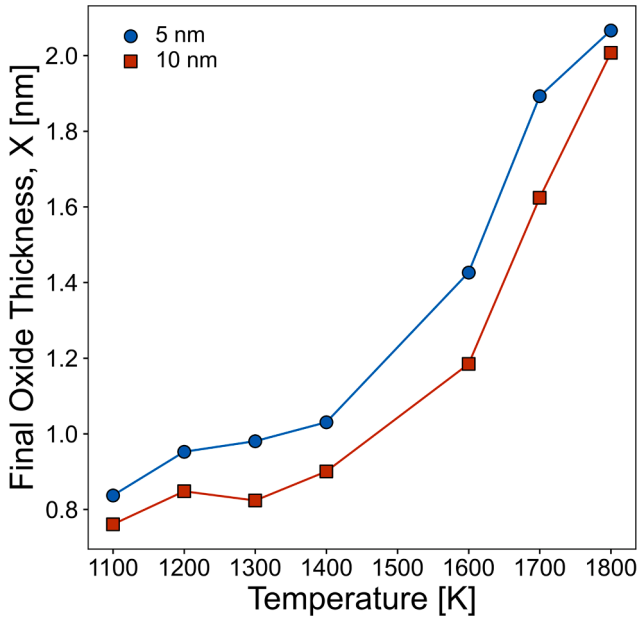

Fig. 7. Effect of grain size on final Si oxide thickness reached after 200 ps.

Tersoff) demonstrate that surface melting initiates in SiC well below the melting temperature and proceeds gradually [38–40], which is consistent with our own observations. For $T \leq 1500$ K, activation energies of 19.17 kJ/mol and 22.14 kJ/mol are obtained for the 5-nm and 10-nm nanocrystals, respectively, with $R^2 > 95\%$ in both cases. Apparently, the introduction of a grain-boundary network produced a two-fold decrease in activation energies compared to our monocrystalline SiC results at $T \leq 1500$ K. We find that the activation energy for the 5-nm nanocrystalline sample is 2.97 kJ/mol lower than for the 10-nm sample, while the grain-boundary atom fractions are, respectively, 4.6% and 1.3%. For $T \geq 1500$ K, the activation energies in Fig. 6 are found to substantially rise to 126.58 kJ/mol and 166.95 kJ/mol for the 5-nm and 10-nm nanocrystalline models, respectively. These findings therefore reveal a radical change in oxidation kinetics in nanocrystalline SiC at temperatures above 1500 K, but not in monocrystalline SiC, which suggests fundamentally different oxidation mechanisms.

A representation of the final oxide thickness reached by the nanocrystals after 200 ps of oxygen exposure is shown in Fig. 7. It indicates that a moderate increase of grain-boundary fraction due to grain refinement does uniformly increase the oxide thickness over the entire range of temperatures. On one hand, this result is consistent with the conclusions of Liu et al. [25] who have predicted that an incoherent GB locally accelerates the growth of oxide in monocrystalline SiC at 2000 K due to enhanced grain-boundary reactions. On the other hand, the fact

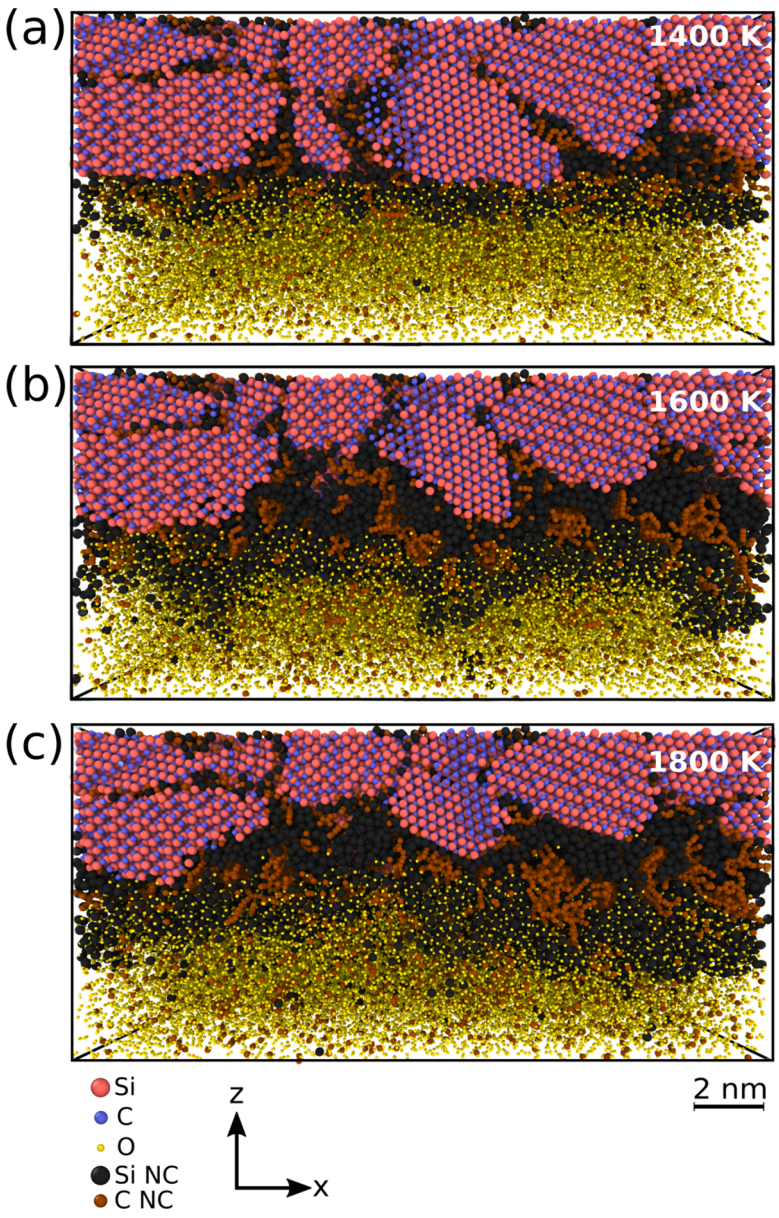

Fig. 8. Snapshots of a nanocrystalline 3C-SiC film with a mean grain diameter of 5 nm after 200 ps at various annealing temperatures from 1400 K to 1800 K. Non-crystalline (NC) Si and C atoms have been highlighted in darker colors for clarity.

that the change is uniform at all temperatures is indicative that, in our simulations, grain boundaries are not directly responsible for the oxidation kinetics transition predicted in nanocrystalline SiC.

To better understand why two oxidation regimes exist in nanocrystalline SiC, Fig. 8 presents the effect of oxidation temperature (1400 K – 1800 K) on the atomic configuration after 200 ps in the 5-nm nanocrystalline model. The dynamics over the full 200 ps of simulation are provided for three temperatures in Supplementary Movies S2-S4. At $T = 1400$ K, we find that a smooth Si oxide layer is formed across the entire interface. The oxide layer consists of SiOx and CO molecules with a CO gas separating away to the oxygen reservoir. From the dynamics of oxygen atoms, we do not observe any preferential diffusion of oxygen along grain boundaries, and no significant change in the shape of the grain boundary network throughout the simulation (Supplementary Movie S2).

Remarkably, at $T = 1600$ K, we find the formation and growth of a liquid Si layer at the interface between SiC grain boundaries and the SiOx oxide (Supplementary Movie S3). The grain boundaries at the oxide interface melt and atomically segregate into pure Si and C clusters. As the temperature is increased to $T = 1800$ K, the liquid Si regions continue to grow by taking over adjacent crystalline grains (Supplementary Movie S4). Two peculiar characteristics are noteworthy in this process. First, although interfacial melting is observed, the bulk material remains primarily crystalline up to 1800 K, suggesting that surface melting is a by-product of active oxidation mechanisms. Second, Fig. 4 (c) displays no significant oxygen diffusion through the liquid Si phase even at the highest temperature, which gives credence for active oxidation between the SiOx scale and the SiC grain boundaries.

Although the global system temperature is held constant, substantial thermal gradients could develop internally. To quantify this effect, the average temperature as a function of the z-coordinate (along the oxidation direction) is presented in Fig. 9 for the SiC nanocrystal with an average grain diameter of 5 nm at several global temperature targets. In the region where atomic oxygen atoms are introduced (-5 nm$\leq z \leq -1.5$ nm), the temperature is constant and adheres closely to the target value. However, near the SiC crystal surface ($z = 0$ nm), the temperature increases, reaching a maximum within $0 \leq z \leq 2$ nm (at approximately the SiC/SiOx interface) before gradually decreasing to satisfy the frozen

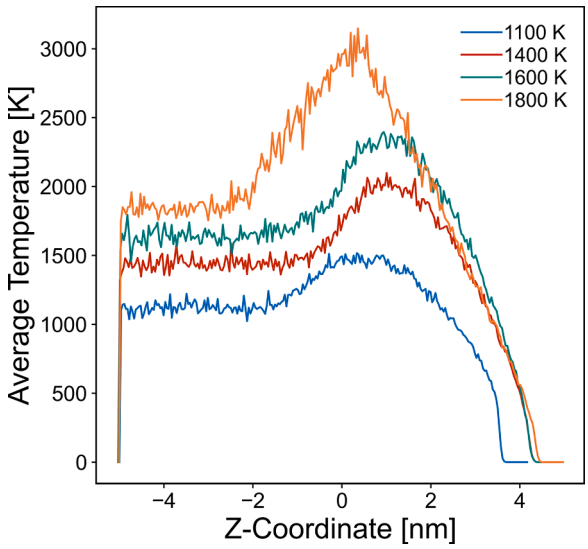

Fig. 9. Average temperature profiles along the oxidation direction for the SiC nanocrystalline model with an average grain diameter of 5 nm. A Z-coordinate of zero corresponds to the coordinate of the initial gas-solid interface.

boundary condition at $z = 5$ nm.

Here, an increase in thermal energy inside the crystal is necessary to satisfy both the global temperature restriction and the boundary condition. Peak temperatures are 50% and 75% higher than the corresponding target temperatures of 1400 K and 1800 K. This reveals that the melting point of the bulk crystal is only exceeded for the highest temperature simulations rather than at 1500 K where we observe a transition in oxidation kinetic. This further confirms that the observed surface melting is primarily a byproduct of active oxidation mechanisms.

4. Discussion

4.1. Static versus dynamic oxygen reservoirs

Past experiments on oxidation resistance [41–48], mechanical stability [49–51], and ablation characteristics [52,53] of SiC fiber-reinforced composites and woven SiC fiber materials have shown pronounced reductions in tensile strength, fatigue, and creep resistance after exposure to high-temperature air and oxygen environments [14, 54–57]. This effect is found to be compounded by the dissociated atomic oxygen encountered at low pressure and very high flow rates when SiC is used in atmospheric re-entry conditions [5,15]. These dynamic conditions are profoundly different from static heating of SiC in a standard air environment [14]. Therefore, it is physically meaningful to find differences in the oxidation behavior of SiC between static and dynamic oxygen reservoir conditions in the present study.

In the monocrystal simulations using a static oxygen reservoir, most C atoms in the SiC matrix are transported to the gas reservoir as CO and CO_2 molecules. The formation of clumped C chains within the SiOx layer is indicative that the diffusive driving force is quickly overcome by viscous forces once the C molecule grows sufficiently large. The snapshots in Fig. 4b show that the reactions at 2000 K occur in the very first 20 ps of annealing. However, the rate on the C(100) face is partially suppressed because the C terminations must first react and be transported away from the surface. This allows the Si(100) crystal to successfully compete for the available reactants in the static oxygen reservoir. This observation proves that a static oxygen reservoir condition is not viable for multi-grain simulations, because this study finds that the surface characteristics of certain orientations artificially dominate the reaction with the available reactants in the reservoir.

Furthermore, it is worth noting in Fig. 5 that the final oxide thicknesses reached in conditions below 1500 K are relatively higher in the monocrystalline models than in their nanocrystalline counterparts. Apparently, this result is counterintuitive because this study concludes that the introduction of a grain-boundary network tends to accelerate active oxidation rates. We attribute this anomaly to the oxygen introduction technique used to replenish the dynamic reservoir. Oxygen atoms are introduced at random positions within the gas reservoir, whose dimensions are determined by the respective model. Since the monocrystals are much smaller than the nanocrystalline models, a given oxygen atom must be transported over significantly shorter distances before reaching the SiC interface, hence the enhanced oxidation kinetics. Nevertheless, we find that this difference is diminished at higher temperatures because active oxidation of monocrystalline and nanocrystalline SiC under dynamic oxygen reservoirs proves to be dominated by equilibrium reactions at the interface between Si oxide scale and crystalline SiC, rather than by direct reactions with oxygen atoms.

4.2. Oxidation mechanisms in nanocrystalline SiC

Several aspects of the present study provide fundamentally new insights into the roles of a grain-boundary network on active oxidation mechanisms in SiC. First, MD simulations are a particularly valuable tool for directly studying chemical interactions at very short time scales where experiments are technologically challenging. The ReaxFF interatomic potential [58,67] is parameterized using ab initio calculations and experimental data, which allows for quantum mechanical calculations to be accurately reproduced for substantially larger atomic systems [59,60]. These potentials have been widely used to study the oxidation of 3C-SiC surfaces by O_2 and H_2O at temperatures up to 5000 K [16,26], and the roles of crystal orientation [27,28,22,36,31], point defects [60], geometry [61], and atomic oxygen collisions [23] upon monocrystalline SiC oxidation. Liu et al. [25] have extended this approach to bicrystals containing both coherent and incoherent grain boundaries to investigate the physical origin of growth rate enhancements observed experimentally [62–64]. However, the present study is the first to systematically examine the effects of a grain-boundary network on active oxidation kinetics in SiC with grains on the order of 5–10 nm [17].

Second, from the two distinct oxidation kinetics predicted in nanocrystalline SiC, a higher activation energy above 1500 K indicates that the underlying chemical process is more kinetically driven than diffusion controlled at high temperature. Diffusion controlled processes generally have activation energies on the order of 15–20 kJ/mol [65], whereas higher activation energies suggest that the oxidation rates are limited by the chemical reaction. In fact, our results reveal that oxygen diffusion is blocked by a layer of liquid Si forming at the oxide/crystalline interface at temperatures above 1500 K. Although atom diffusion could not be properly simulated over only 200 ps, this conclusion is supported by the work of Silva et al. [66], which found that amorphous Si has less reactivity and less diffusion transport of oxygen than crystalline Si.

Third, in active oxidation studies, the transition points from passive-to-active reactions are critical for understanding the rates of oxidation and the roles of microstructures on SiC oxidation [41,15]. The different active oxidation mechanisms in SiC have been summarized by Jacobsen et al. [15] through four possible equilibrium reactions and associated phase transformations:

$$SiC(s) + O_2(g) = SiO(g) + CO(g) \quad (3a)$$

$$SiC(s) + 2SiO_2(s) = 3SiO(g) + CO(g) \quad (3b)$$

$$SiC(s) + SiO_2(s) = 2SiO(g) + C(s) \quad (3c)$$

$$2SiC(s) + SiO_2(g) = 3Si(l, s) + 2CO(g) \quad (3d)$$

From our simulations, the formation of clumped C clusters in the oxide layer agrees with the product of reaction (3c), suggesting that

Table 1
Elemental participation in different equilibrium reactions for active oxidation of SiC.

Oxidation Reaction	Si (wt.%)	C (wt.%)	O (wt.%)
(3a)	39	17	44
(3b)	53	7	40
(3c)	56	12	32
(3d)	60	17	23
Oxygen plasma experiment (Fig. 1)	*48*	*20*	*32*

active oxidation is governed by this type of reaction in the monocrystalline C(100) up to 2000 K and the nanocrystalline SiC samples up to 1500 K. In monocrystalline Si(100) at 2000 K and nanocrystalline samples above 1500 K, the appearance of a pure non-crystalline Si layer in the oxide interface matches well with the products of reaction (3d). This conclusion is consistent with past experimental observations of SiC in dissociated oxygen [5] showing that, at constant oxygen pressure, reaction (3d) only achieves thermodynamic equilibrium at higher temperatures than reaction (3c).

To test the above hypothesis, we compared the chemical analysis of Fiber A from the experiment in Fig. 1 to the elemental participation in each equilibrium reaction. Table 1 shows the oxygen composition of Fiber A is closer to the oxygen participation involved with reaction (3c). Interestingly, Fiber B in Fig. 1 shows clear signs of surface melting, which could also be attributed to the liquid Si phase produced in reaction (3d). Since the surface temperature measurement fluctuated at 1573 ± 50 K on those fibers, it is possible that both reactions (3c) and (3d) coexisted under the testing conditions. In summary, our simulation and experimental evidence suggests that the grain-boundary network facilitated the formation and stability of a liquid Si phase at the interface where grain boundaries intersected with the Si oxide. In turn, this reaction kinetically changed the active oxidation process.

5. Conclusions

We performed large-scale reactive MD simulations of monocrystalline and nanocrystalline 3C-SiC oxidation up to 2000 K. The conditions within the oxygen reservoir were found to strongly influence the oxidation kinetics and underlying equilibrium reactions. Under static conditions, certain orientations dominated the reactions with the available reactants and produced oxidation trajectories that were not physically accurate. A dynamic condition whereby oxygen atoms were continuously introduced to the system, was found to be more reliable for large-scale computational studies. It is demonstrated that active oxidation occurs at the interface between the crystalline SiC and Si oxide at all temperatures. However, temperature-dependent simulations of nanocrystalline SiC revealed two distinct oxidation regimes, with a critical transition at $T = 1500$ K, which differed from monocrystalline SiC. A key finding is the prediction of surface melting for $T > 1500$ K, supported by experimental evidence, stemming from the formation of a liquid Si phase at the SiC/Si oxide interface. It is shown that the stability of the interfacial liquid phase is promoted by incoherent grain boundaries in the crystalline SiC. This study underscores a critical design consideration for the deployment of nanocrystalline SiC fibers for high-temperature applications, emphasizing the need for further large-scale atomistic simulations.

Declaration of Competing Interest

The authors declare that they have no known competing financial interests or personal relationships that could have appeared to influence the work reported in this paper.

Acknowledgement

We thank Drs. Jason Meyers and Rodrigo Penide-Fernandez for helpful discussion at the initial stage of this research. This research received support by the U.S. Department of Energy (DOE) under grant No. DE-SC0020054 and used computational resources from the Extreme Science and Engineering Discovery Environment (XSEDE) supported by the National Science Foundation (NSF) under grant no. ACI-1548562 and the National Energy Research Scientific Computing Center (NERSC), a U.S. DOE Office of Science User Facility operated under contract no. DE-AC02-05CH11231. The field-emission SEM and EDS spectrometer were acquired through NSF MRI grant no. 1828371. LC gratefully acknowledges support from the NSF Graduate Research Fellowship Program under grant No. DGE-1845298, the Vermont Space Grant Consortium under award No. 29907 and the Department of Mechanical Engineering at the University of Vermont.

Supplementary materials

Supplementary material associated with this article can be found, in the online version, at doi:10.1016/j.actamat.2023.119229.

References

[1] T. Koyanagi, Y. Katoh, T. Nozawa, Design and strategy for next-generation silicon carbide composites for nuclear energy, J. Nucl. Mater. 540 (2020), 152375, https://doi.org/10.1016/j.jnucmat.2020.152375.
[2] K. Jacobs, S. Heinig, D. Johannesson, S. Norrga, H. Nee, Comparative evaluation of voltage source converters with silicon carbide semiconductor devices for high-voltage direct current transmission, IEEE Trans. Power Electron. 36 (2021) 8887–8906, https://doi.org/10.1109/TPEL.2021.3049320.
[3] J. Roy, S. Chandra, S. Das, S. Maitra, Oxidation behavior of silicon carbide - a review, Rev. Adv. Mater. Sci. 38 (2014) 29–39.
[4] T. Zang, A. Dwyer-Cianciolo, M. Ivanov, R. Sostaric, D. Kinney, Overview of the NASA entry, descent and landing systems analysis studies for large robotic-class missions, in: Proceedings of the AIAA SPACE Conference & Exposition, 2012, https://doi.org/10.2514/6.2011-7294.
[5] B. Berton, M.P. Bacos, D. Demange, J. Lahaye, High-temperature oxidation of silicon carbide in simulated atmospheric re-entry conditions, J. Mater. Sci. 27 (2005) 3206–3210, https://doi.org/10.1007/bf01116013.
[6] J. Del Corso, Flexible thermal protection system development for hypersonic inflatable aerodynamic decelerators, in: Proceedings of the 9th International Planetary Probe Workshop, 2012.
[7] S. Hughes, F. Cheatwood, R. Dillman, A. Calomino, H. Wright, J. DelCorso, A. Calomino, Hypersonic Inflatable Aerodynamic Decelerator (HIAD) technology development overview, in: Proceedings of the 21st AIAA Aerodynamic Decelerator Systems Technology Conference and Seminar, 2012.
[8] National Wildfire Coordinating Group, Fire shelter history. https://www.nwcg.gov/publications/pms411/fire-shelter-history (accessed 23.05.2002).
[9] M. Wusk, A. Calomino, K. Daryabeigi, W. Bruce, J. Fody, S. Miller and S. Vague, Lightweight flexible thermal protection system for fire protection. U.S. Patent No. 10300675B2 (2019).
[10] P. Dennison, K. Charoensiri, D. Roberts, S. Peterson, R. Green, Wildfire temperature and land cover modeling using hyperspectral data, Remote Sens. Environ. 100 (2005) 212–222, https://doi.org/10.1016/j.rse.2005.10.007.
[11] G. Chapline, A. Rodriguez, C. Snapp, G. Dorsey, M. Fowler, B. Greene, W. Schneider, C. Scott, M. Pessin, J. Butler, Thermal protection systems. Wings in Orbit, CreateSpace Independent Publishing Platform, 2011, pp. 182–200.
[12] G. Swanson, B. Smith, R. Akamine, R. Bodkin, N. Cheatwood, A. Parker, S. Hughes, D. Gaddy, The HIAD orbital flight demonstration instrumentation suite, in: Proceedings of the International Planetary Probe Workshop, 2018.
[13] G. Chollon, R. Pailler, R. Naslain, F. Laanani, M. Monthioux, P. Olry, Thermal stability of a PCS-derived SiC fibre with a low oxygen content (Hi-Nicalon), J. Mater. Sci. 32 (2) (1997) 327–347, https://doi.org/10.1023/a:1018541030308.
[14] W. Owens, D. Merkel, F. Sansoz, D. Fletcher, Fracture behavior of woven silicon carbide fibers exposed to high-temperature nitrogen and oxygen plasmas, J. Am. Ceram. Soc. 98 (2005) 4003–4009, https://doi.org/10.1111/jace.13826.
[15] N.S. Jacobson, D.L. Myers, B.J. Harder, Active oxidation of silicon carbide, Mater. High Temp. 29 (2012) 193–198, https://doi.org/10.3184/096034012x13322284984793.
[16] D.A. Newsome, D. Sengupta, H. Foroutan, M.F. Russo, A.C.T. van Duin, Oxidation of silicon carbide by O_2 and H_2O: a ReaxFF reactive molecular dynamics study, part I, J. Phys. Chem. C 116 (2012) 16111–16121, https://doi.org/10.1021/jp306391p.
[17] H. Ichikawa, T. Ishikawa, 1.6 silicon carbide fibers (Organometallic pyrolysis), Compr. Compos. Mater. II (2017) 127–166, https://doi.org/10.1016/b978-0-08-100533-0.00042-7.
[18] S. Plimpton, Fast parallel algorithms for short-range molecular dynamics, J. Comput. Phys. 117 (2002) 1–19, https://doi.org/10.1006/jcph.1995.1039.

[19] A. Vashisth, S. Khatri, S.H. Hahn, W. Zhang, A.C.T. van Duin, M. Naraghi, Mechanical size effects of amorphous polymer-derived ceramics at the nanoscale: experiments and ReaxFF simulations, Nanoscale 11 (2019) 7447–7456, https://doi.org/10.1039/C9NR00958B.

[20] W. Zhang, A.C.T. van Duin, Improvement of the ReaxFF description for functionalized hydrocarbon/water weak interactions in the condensed phase, J. Phys. Chem. B 122 (14) (2018) 4083–4092, https://doi.org/10.1021/acs.jpcb.8b01127.

[21] M.C. Pitman, A.C.T. van Duin, Dynamics of confined reactive water in smectite clay–zeolite composites, J. Am. Chem. Soc. 134 (6) (2012) 3042–3053, https://doi.org/10.1021/ja208894m.

[22] T. Park, C. Park, J. Jung, G.J. Yun, Investigation of silicon carbide oxidation mechanism using ReaxFF molecular dynamics simulation, J. Spacecr. Rockets 57 (2020) 1328–1334, https://doi.org/10.2514/1.a34669.

[23] Z. Cui, J. Zhao, G. Yao, Z. Li, D. Wen, Molecular insight of the interface evolution of silicon carbide under hyperthermal atomic oxygen impact, Phys. Fluids 34 (2022), 052101, https://doi.org/10.1063/5.0092005.

[24] P. Hirel, Atomsk: a tool for manipulating and converting atomic data files, Comput. Phys. Commun. 197 (2015) 212–219, https://doi.org/10.1016/j.cpc.2015.07.012.

[25] C. Liu, J. Xi, I. Szlufarska, Sensitivity of SiC grain boundaries to oxidation, J. Phys. Chem. C 123 (2019) 11546–11554, https://doi.org/10.1021/acs.jpcc.9b00068.

[26] D.A. Newsome, D. Sengupta, A.C.T. van Duin, High-temperature oxidation of SiC-based composite: rate constant calculation from ReaxFF MD simulations, Part II, J. Phys. Chem. C 117 (2013) 5014–5027, https://doi.org/10.1021/jp307680t.

[27] Y. Sun, Y. Liu, F. Xu, ReaxFF molecular dynamics study on oxidation behavior of 3C-SiC: polar face effects, Chin. Phys. B 24 (2015), 096203, https://doi.org/10.1088/1674-1056/24/9/096203.

[28] V. Šimonka, A. Hössinger, J. Weinbub, S. Selberherr, ReaxFF reactive molecular dynamics study of orientation dependence of initial silicon carbide oxidation, J. Phys. Chem. A 121 (2017) 8791–8798, https://doi.org/10.1021/acs.jpca.7b08983.

[29] E. Maras, O. Trushin, A. Stukowski, T. Ala-Nissila, H. Jónsson, Global transition path search for dislocation formation in Ge on Si(001), Comput. Phys. Commun. 205 (2016) 13–21, https://doi.org/10.1016/j.cpc.2016.04.001.

[30] A. Stukowski, Visualization and analysis of atomistic simulation data with OVITO–the open visualization tool, Model. Simul. Mater. Sci. Eng. 18 (2009), 015012, https://doi.org/10.1088/0965-0393/18/1/015012.

[31] Z. Chen, Z. Sun, X. Chen, Y. Wu, X. Niu, Y. Song, ReaxFF reactive molecular dynamics study on oxidation behavior of 3C-SiC in H_2O and O_2, Comput. Mater. Sci. 195 (2021), 110475, https://doi.org/10.1016/j.commatsci.2021.110341.

[32] M. Wilson, E. Opila, A review of SiC fiber oxidation with a new study of Hi-nicalon SiC fiber oxidation, Adv. Eng. Mater. 18 (2016) 1698–1709, https://doi.org/10.1002/adem.201600166.

[33] H.Z. Massoud, J.D. Plummer, E.A. Irene, Thermal oxidation of silicon in dry oxygen: accurate determination of the kinetic rate constants, J. Electrochem. Soc. 132 (1985) 1745–1753, https://doi.org/10.1149/1.2114204.

[34] V. Šimonka, A. Hössinger, J. Weinbub, S. Selberherr, Growth rates of dry thermal oxidation of 4H-silicon carbide, J. Appl. Phys. 120 (2016), 135705, https://doi.org/10.1063/1.4964688.

[35] R. Penide-Fernandez, F. Sansoz, Microscale knudsen effect over the transverse thermal conductivity of woven ceramic fabrics under compression, Int. J. Heat Mass Transf. 171 (2021), 121085, https://doi.org/10.1016/j.ijheatmasstransfer.2021.121085.

[36] X. Chen, Z. Sun, Z. Chen, Y. Song, X. Niu, ReaxFF molecular dynamics simulation of oxidation behavior of 3C-SiC in O_2 and CO_2, Comput. Mater. Sci. 191 (2021), 110341, https://doi.org/10.1016/j.commatsci.2021.110341.

[37] M.Q. Brisebourg, F. Rebillat, F. Teyssandier, Oxidation of ß-SiC at high temperature in Ar/O_2, Ar/CO_2, Ar/H_2O gas mixtures: kinetic study of the silica growth in the passive regime, J. Eur. Ceram. Soc. 38 (2018) 4309–4319, https://doi.org/10.1016/j.jeurceramsoc.2018.05.029.

[38] H.T.T. Nguyen, Structural evolution of SiC sheet in a graphene-based in-plane hybrid system upon heating using molecular dynamics simulation, Thin Solid Films 739 (2021), 138992, https://doi.org/10.1016/j.tsf.2021.138992.

[39] D.T.N. Tranh, V.V. Hoang, T.T.T. Hanh, Modeling glassy SiC nanoribbon by rapidly cooling from the liquid: an affirmation of appropriate potentials, Physica B 608 (2021), 412746, https://doi.org/10.1016/j.physb.2020.412746.

[40] V.V. Hoang, Melting and pre-melting of two-dimensional crystalline SiC nanoribbons, Physica E 137 (2022), 115012, https://doi.org/10.1016/j.physe.2021.115012.

[41] J. Han, P. Hu, X. Zhang, S. Meng, W. Han, Oxidation-resistant ZrB_2–SiC composites at 2200°C, Compos. Sci. Technol. 68 (2007) 799–806, https://doi.org/10.1016/j.compscitech.2007.08.017.

[42] H. Hatta, T. Aoki, Y. Kogo, T. Yarii, High-temperature oxidation behavior of SiC-coated carbon fiber-reinforced carbon matrix composites, Compos. Part A 30 (2002) 515–520, https://doi.org/10.1016/s1359-835x(98)00143-2.

[43] F. Monteverde, R. Savino, M.D.S. Fumo, A. Di Maso, Plasma wind tunnel testing of ultra-high temperature ZrB_2-SiC composites under hypersonic re-entry conditions, J. Eur. Ceram. Soc. 30 (2010) 2313–2321, https://doi.org/10.1016/j.jeurceramsoc.2010.01.029.

[44] K.S. Cissel, E. Opila, Oxygen diffusion mechanisms during high-temperature oxidation of ZrB_2-SiC, J. Am. Ceram. Soc. 101 (2017) 1765–1779, https://doi.org/10.1111/jace.15298.

[45] K. Shugart, E. Opila, SiC depletion in ZrB_2–30 vol% SiC at ultrahigh temperatures, J. Am. Ceram. Soc. 98 (2015) 1673–1683, https://doi.org/10.1111/jace.13519.

[46] K. Shugart, S. Liu, F. Craven, E. Opila, Determination of retained B_2O_3 content in ZrB_2-30 vol% SiC oxide scales, J. Am. Ceram. Soc. 98 (2014) 287–295, https://doi.org/10.1111/jace.13236.

[47] K. Shugart, B. Patterson, D. Lichtman, S. Liu, E. Opila, Mechanisms for variability of ZrB2-30 vol% SiC oxidation kinetics, J. Am. Ceram. Soc. 97 (2014) 2279–2285, https://doi.org/10.1111/jace.12911.

[48] K. Shugart, W. Jennings, E. Opila, Initial stages of ZrB2-30 vol% SiC oxidation at 1500 °C, J. Am. Ceram. Soc. 97 (2014) 1645–1651, https://doi.org/10.1111/jace.12843.

[49] F. Monteverde, R. Savino, Stability of ultra-high-temperature ZrB_2–SiC ceramics under simulated atmospheric re-entry conditions, J. Eur. Ceram. Soc. 27 (2007) 4797–4805, https://doi.org/10.1016/j.jeurceramsoc.2007.02.201.

[50] E.J. Opila, M.K. Boyd, Oxidation of SiC fiber-reinforced SiC matrix composites with a BN interphase, Mater. Sci. Forum 696 (2011) 342–347, https://doi.org/10.4028/www.scientific.net/msf.696.342.

[51] A. Purwar, V. Thiruvenkatam, B. Basu, Experimental and computational analysis of thermo-oxidative-structural stability of ZrB_2-SiC-Ti during arc-jet testing, J. Am. Ceram. Soc. 100 (10) (2017) 4860–4873, https://doi.org/10.1111/jace.15001.

[52] T. Ogasawara, T. Aoki, M.S.A. Hassan, Y. Mizokami, N. Watanabe, Ablation behavior of SiC fiber/carbon matrix composites under simulated atmospheric reentry conditions, Compos. Part A 42 (2010) 221–228, https://doi.org/10.1016/j.compositesa.2010.10.015.

[53] X. Zhang, P. Hu, J. Han, S. Meng, Ablation behavior of ZrB2–SiC ultra high temperature ceramics under simulated atmospheric re-entry conditions, Compos. Sci. Technol. 68 (2008) 1718–1726, https://doi.org/10.1016/j.compscitech.2008.02.009.

[54] M. Takeda, Y. Imai, H. Ichikawa, Y. Kagawa, H. Iba, H. Kakisawa, Some mechanical properties of Sic(Hinicalon™) fiber-reinforced sic matrix nicaloceram™ composites, in: Proceedings of the 21st Annual Conference on Composites, Advanced Ceramics, Materials, and Structures 18, 2008, pp. 779–784, https://doi.org/10.1002/9780470294437.ch85.

[55] R.S. Hay, P. Mogilevsky, Model for SiC fiber strength after oxidation in dry and wet air, J. Am. Ceram. Soc. 102 (2018) 397–415, https://doi.org/10.1111/jace.15907.

[56] Y. Chai, X. Zhou, H. Zhang, Effect of oxidation treatment on KD–II SiC fiber–reinforced SiC composites, Ceram. Int. 43 (2017) 9934–9940, https://doi.org/10.1016/j.ceramint.2017.05.001.

[57] Z. Liu, J.M. Meyers, J. Schindler, F. Sansoz, T. Tan, D.G. Fletcher, *In situ* tensile behavior of Hi-Nicalon silicon carbide fibers exposed to high-temperature argon plasma, J. Am. Ceram. Soc. 105 (2021) 525–537, https://doi.org/10.1111/jace.18073.

[58] A.C.T. van Duin, S. Dasgupta, F. Lorant, W.A. Goddard, ReaxFF: a reactive force field for hydrocarbons, J. Phys. Chem. A 105 (2002) 9396–9409, https://doi.org/10.1021/jp004368u.

[59] T.P. Senftle, S. Hong, M.M. Islam, S.B. Kylasa, Y. Zheng, Y.K. Shin, C. Junkermeier, R. Engel-Herbert, M.J. Janik, H.M. Aktulga, T. Verstraelen, A. Grama, A.C.T. van Duin, The ReaxFF reactive force-field: development, applications and future directions, NPJ Comput. Mater. 2 (2016), https://doi.org/10.1038/npjcompumats.2015.11.

[60] J. Xi, C. Liu, I. Szlufarska, Effects of point defects on oxidation of 3C–SiC, J. Nucl. Mater. 538 (2020), 152308, https://doi.org/10.1016/j.jnucmat.2020.152308.

[61] H. Gao, H. Wang, M. Niu, L. Su, X. Fan, J. Wen, Y. Wei, Oxidation simulation study of silicon carbide nanowires: a carbon-rich interface state, Appl. Surf. Sci. 493 (2019) 882–888, https://doi.org/10.1016/j.apsusc.2019.07.016.

[62] L. Tan, T. Allen, E. Barringer, Effect of microstructure on the corrosion of CVD-SiC exposed to supercritical water, J. Nucl. Mater. 394 (2009) 95–101, https://doi.org/10.1016/j.jnucmat.2009.08.008.

[63] S. Tsurekawa, T. Watanabe, N. Tamari, Grain boundary engineering for the control of mechanical properties and oxidation-induced embrittlement in silicon carbides, Key Eng. Mater. 261-263 (2009) 999–1004, https://doi.org/10.4028/www.scientific.net/kem.261-263.999.

[64] S. Tsurekawa, H. Watanabe, N. Tamari, T. Watanabe, Improvement of oxidation resistance and oxidation-induced embrittlement by controlling grain boundary microstructure in silicon carbides with different dopants, Mater. Trans. 45 (7) (2005) 2128–2136, https://doi.org/10.2320/matertrans.45.2128.

[65] J. Kelly, J. Meerakker, P. Notten, R. Tijburg, Wet-chemical etching of III-V semiconductors, Philips Tech. Rev. 44 (3) (1988) 61–74.

[66] A.G. Silva, K. Pedersen, Z.S. Li, P. Morgen, Oxidation of the surface of a thin amorphous silicon film, Thin Solid Films 520 (2011) 697–699, https://doi.org/10.1016/j.tsf.2011.04.189.

[67] K. Chenoweth, A.C.T. van Duin, W.A. Goddard, ReaxFF reactive force field for molecular dynamics simulations of hydrocarbon oxidation, J. Phys. Chem. A 112 (2008) 1040–1053, https://doi.org/10.1021/jp709896w.